



Cite this: *Dalton Trans.*, 2024, **53**, 16577

Broadband blue light emissions of one-dimensional hybrid Cu(I) halides with ultrahigh anti-water stability†

Na Lin,^{a,b} Yun-Xia Li,^a Yu Liu,^a Kai-Qi Sun,^a Hong-Yan Zhang,^a Xiao-Wu Lei *^a and Zhi-Wei Chen *^a

Low-dimensional organic–inorganic hybrid lead halide perovskites have attracted much interest in solid-state lighting and displays, but the toxicity and instability of lead halide are obstacles to their industrial applications, which must be overcome. As an alternative, Cu(I)-based hybrid metal halides have emerged as a new type of luminescent material owing to their diversified structure, adjustable luminescence, low toxicity and low cost. Herein, we report three one-dimensional (1D) hybrid Cu(I)-based halides with the general formula ACu_2Br_4 ($A = [(Me)_4\text{-Pipz}]^{2+}$ and $[BuDA]^{2+}$ and $[TMEDA]^{2+}$). These 1D hybrid Cu(I) halides display stable broadband blue emission with maximum emission peaks in the range of 445–474 nm and the highest photoluminescence quantum yield of 37.8%. Furthermore, in-depth experimental and theoretical investigations revealed that the broadband blue emissions originate from the radiative recombination of self-trapped excitons. Most importantly, there is no structural degradation and attenuation of emission intensity even after continuously soaking these halides in water for at least two months, demonstrating their ultra-high anti-water stability. Hirshfeld surface analysis shows that a large number of weak hydrogen bonds can protect the inorganic skeleton from degradation due to water. This work provides a new strategy for the design of water-stable Cu(I)-based halides with efficient blue emission and wide potential applications in humid environments.

Received 18th July 2024,
Accepted 18th September 2024

DOI: 10.1039/d4dt02072c

rsc.li/dalton

1. Introduction

Three-dimensional (3D) perovskite nanocrystals (PNCs) with the general formula $APbX_3$ ($A = Cs^+$, FA^+ and MA^+ ; $X = Cl$, Br , and I) have emerged as a new type of photoluminescent materials owing to their exceptional optoelectronic properties of strong absorption coefficient, high photoluminescence quantum yield (PLQY), narrow full width at half-maximum (FWHM), adjustable optical bandgap and long carrier diffusion.^{1–3} Nevertheless, 3D NCs suffer from intrinsic instability in humid air and toxicity of Pb^{2+} , which prevents their further commercial applications.⁴ Thus, it is crucial to develop new type of stable lead-free photoluminescent materials with desirable properties comparable to perovskites.

Recently, low-dimensional organic–inorganic metal halides (OIMHs), which were derived from 3D bulk perovskites $APbX_3$

using large organic cations to replace the A-site, have captured tremendous attention from researchers because of their adjustable structures and multifunctional optical/electronic applications such as the fabrication of light-emitting diodes (LEDs), X-ray scintillators, luminescence sensors and lasers.^{5–8} Remarkably, versatile large organic cations and abundant lead-free metal ions allow OIMHs to deliver two-dimensional (2D), one-dimensional (1D) and zero-dimensional (0D) structures based on the spatial arrangement of anionic inorganic and cationic organic species, resulting in various crystal structures and tunable photophysical properties.^{9–11} Among these low-dimensional OIMHs, 1D hybrid metal halides feature richer structures constructed by connecting metal polyhedra through corner-, edge-, and face-sharing compared with 3D perovskites. In 1D hybrid metal halides, organic cations and inorganic metal–halogen anions are spatially independent with strong intrinsic quantum confinement, which endow 1D halides with an ultrahigh PLQY and optical stability in single crystals. Compared with the narrow light emission of 3D perovskites, the soft crystal lattice of 1D halides is prone to structural deformation in the excited state, which easily results in self-trapped excitons.¹² Therefore, 1D OIMHs tend to display STE-associated broadband light emissions with potential applications in solid-state white lighting and display diodes.

To date, numerous low-dimensional OIMHs have been reported in multifunctional applications with broadband emis-

^aResearch institute of Optoelectronic Functional Materials, School of Chemistry, Chemical Engineering and Materials, Jining University, Qufu, Shandong, 273155, P. R. China. E-mail: xwlei_jnu@163.com, zw_chen@jnxu.edu.cn

^bSchool of Chemistry and Chemical Engineering, Qufu Normal University, Qufu, Shandong, 273165, P. R. China

† Electronic supplementary information (ESI) available. CCDC 2367415, 2367417 and 2367419. For ESI and crystallographic data in CIF or other electronic format see DOI: <https://doi.org/10.1039/d4dt02072c>

sions based on In^{3+} , Sb^{3+} , Sn^{2+} , Zn^{2+} and Cu^+ ions. However, most In^{3+} and Sb^{3+} -based halides display lower-energy broadband yellow, orange or red-light emissions, while Sn^{2+} in the tin halides is easily oxidized to Sn^{4+} . In addition, the reported Zn^{2+} -based halides exhibit blue light emission, generally with low luminescence efficiency.^{13–16} Relatively speaking, the Cu(I)-based OIMHs possess multiple advantages of low cost and toxicity, various coordination modes, diversified PL properties and high luminescence efficiency.^{17,18} In general, the copper(I) ion features three kinds of coordination environments from linear two-coordinated $[\text{CuX}_2]^-$ unit, three-coordinated $[\text{CuX}_3]^{2-}$ triangle and four-coordinated $[\text{CuX}_4]^{3-}$ tetrahedron. Under the structural directing action and charge balance effect of versatile organic cations, these basic units act as secondary building blocks to assemble various anionic cuprous halogen moieties, such as $[\text{CuX}_2]^-$, $[\text{CuX}_3]^{2-}$, $[\text{CuX}_4]^{3-}$, $[\text{Cu}_2\text{X}_3]^-$, $[\text{Cu}_2\text{X}_4]^{2-}$, $[\text{Cu}_2\text{X}_5]^{3-}$, $[\text{Cu}_3\text{X}_6]^{3-}$, $[\text{Cu}_4\text{X}_6]^{2-}$, $[\text{Cu}_6\text{X}_9]^{3-}$, $[\text{Cu}_6\text{X}_{10}]^{4-}$ and $[\text{Cu}_8\text{X}_{10}]^{2-}$.¹⁹ The fertile coordination structures endow hybrid cuprous halides with adjustable luminescence covering the whole visible spectral range, high PLQY and multiple optoelectronic applications. Accordingly, numerous Cu(I)-based halides have been reported to display diversified coordination modes and highly efficient broadband light emissions, which are widely applied in WLED, sensors and X-ray scintillators. However, it is challenging to realize blue light emission for low-dimensional metal halides due to the large Stokes shift of STE emission. Hence, though numerous Cu(I) halides exhibit red, green, yellow light emissions with high PLQYs, as shown in the previous work, rare blue-emissive Cu(I)-based low-dimensional hybrid halide have been achieved. For example, Xia *et al.* reported that 0D $(\text{C}_8\text{H}_{20}\text{N})_2\text{Cu}_2\text{Br}_4$ single crystals show blue emission centred at 468 nm with a near-unity PLQY of 99.7%, a large Stokes shift of 148 nm, and a good environmental stability along with strong X-ray absorption capability, which can lead to the preparation of a large-sized scintillator screen in nondestructive X-ray imaging.²⁰ However, Cu-based low-dimensional hybrid halides still suffer from serious instability due to the facile oxidation of Cu(I) in the presence of moisture and oxygen.²¹ Thus, stability is still one of the problems that need to be addressed for Cu(I)-based OIMHs.

To date, some Cu(I) hybrid halides have been reported with high stabilities by virtue of the strong π - π interaction of the neighboring cations to protect the anionic units from water, oxygen and polar organic solvents.²² For instance, Xie *et al.* reported a stable 0D $(\text{C}_{20}\text{H}_{20}\text{OP})\text{CuCl}_2$ ($\text{C}_{20}\text{H}_{20}\text{OP}^+$ = (methoxymethyl)triphenylphosphonium) single crystal with excellent water resistance stability for at least 24 h using the protection effect of the large organic cation.²³ Although limited water-stable cuprous halides have been prepared to realize water stability, this successful achievement proves the feasibility of structural design engineering to enhance the intrinsic stability of low-dimensional cuprous halides.

To further expand this crystal structural engineering, we present a series of isostructural 1D hybrid Cu(I) halides that emit highly-efficient broadband blue emissions with the

highest PLQY of 37.8% from the intrinsic STEs. Significantly, these cuprous halides exhibit excellent water-resistance stability benefiting from the surrounding protection effect of organic cations through abundant hydrogen bonding. Our work provides a new structural engineering strategy for the construction of highly water-stable 1D hybrid cuprous halides and application in underwater lighting.

2. Results and discussion

Three isostructural 1D Cu halides of $[(\text{Me})_4\text{-Pipz}]\text{Cu}_2\text{Br}_4$, $[\text{BuDA}]\text{Cu}_2\text{Br}_4$ and $[\text{TMEDA}]\text{Cu}_2\text{Br}_4$ were synthesized through the facile hydrothermal method; the syntheses details are described in the Experimental section, and the detailed crystallographic data are given in Tables S1–S3 (ESI†). Single-crystal X-ray diffraction demonstrates that the three halides crystallized in the monoclinic system but with different space groups. Interestingly, the $[(\text{Me})_4\text{-Pipz}]^{2+}$ cation in $[(\text{Me})_4\text{-Pipz}]\text{Cu}_2\text{Br}_4$ was generated *in situ* from the reaction of piperazine and methanol in acid solvent. Briefly, the *N*-alkylation of piperazine occurred in the presence of CH_3OH to generate the methylated piperazine cation of $[(\text{Me})_4\text{-Pipz}]^{2+}$ and further self-assemble to form $[(\text{Me})_4\text{-Pipz}]\text{Cu}_2\text{Br}_4$; a similar phenomenon was reported in a previous work.²⁴ Furthermore, the $[(\text{Me})_4\text{-Pipz}]\text{Cu}_2\text{Br}_4$ crystal cannot be obtained without the assistance of methanol, which further verifies this conclusion. As shown in Fig. 1a, each Cu(I) atom is coordinated by four Br atoms to form tetrahedral $[\text{CuBr}_4]$ units, which are further connected to form 1D $[\text{Cu}_2\text{Br}_4]^{2-}$ chains in the edge-sharing manner. Moreover, the isolated $[\text{Cu}_2\text{Br}_4]^{2-}$ chains periodically embed in the organic cationic matrices of $[(\text{Me})_4\text{-Pipz}]^{2+}$, $[\text{BuDA}]^{2+}$ and $[\text{TMEDA}]^{2+}$, finally resulting in hydrogen bond-formed hybrid structures (Fig. 1b–d). The nearest Cu...Cu distance between the adjacent $[\text{Cu}_2\text{Br}_4]^{2-}$ chains was measured to be 6.9 Å, 7.8 Å and 7.2 Å for $[(\text{Me})_4\text{-Pipz}]\text{Cu}_2\text{Br}_4$, $[\text{BuDA}]\text{Cu}_2\text{Br}_4$ and $[\text{TMEDA}]\text{Cu}_2\text{Br}_4$, respectively. These long distances illustrate the absence of electronic interaction between the adjacent $[\text{Cu}_2\text{Br}_4]^{2-}$ chains, which enable the three halides to exhibit the intrinsic properties of the individual $[\text{Cu}_2\text{Br}_4]^{2-}$ chains. Furthermore, slightly varied distortion degrees are observed in the three copper(I) halides. As shown in Fig. S1,† the Cu–Br distances fluctuate in a narrow range of 2.50 Å–2.53 Å and 2.47 Å–2.50 Å for $[(\text{Me})_4\text{-Pipz}]\text{Cu}_2\text{Br}_4$ and $[\text{BuDA}]\text{Cu}_2\text{Br}_4$, respectively, while the $[\text{CuBr}_4]$ tetrahedron features a higher distortion degree, with the Cu–Br distances varying from 2.47 Å to 2.62 Å in $[\text{TMEDA}]\text{Cu}_2\text{Br}_4$. The powder X-ray diffraction (PXRD) patterns of the samples are in good accordance with the simulated results from single crystal, demonstrating the high purity of the bulk samples (Fig. 1e–g).

As shown in the inset photographs of Fig. 2a–c, the synthesized single crystals of the three Cu(I) halides are colorless and transparent under sunlight, indicating almost no absorption in the visible light range. The UV-vis absorption spectra contain large absorption bands in the range of 200–350 nm, and the corresponding bandgaps are calculated to be 4.0 eV,

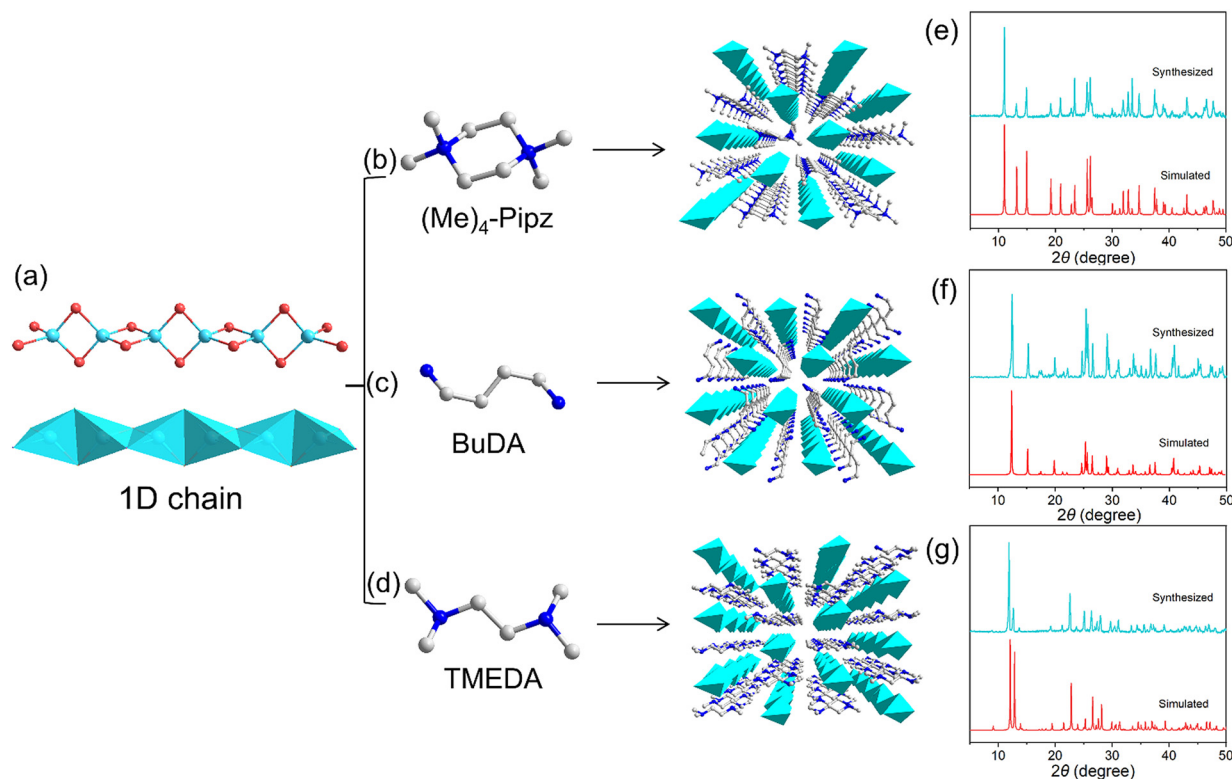


Fig. 1 Crystal structures of three 1D Cu(I) halides: (a) the $[\text{Cu}_2\text{Br}_4]^{2-}$ chain; (b–d) Organic cations and packing structures of $[(\text{Me})_4\text{-Pipz}]\text{Cu}_2\text{Br}_4$, $[\text{BuDA}]\text{Cu}_2\text{Br}_4$ and $[\text{TMEDA}]\text{Cu}_2\text{Br}_4$ (hydrogen atoms were hidden for clarity); (e–g) Simulated and experimental PXRD patterns of three halides.

3.9 eV and 3.8 eV for $[(\text{Me})_4\text{-Pipz}]\text{Cu}_2\text{Br}_4$, $[\text{BuDA}]\text{Cu}_2\text{Br}_4$ and $[\text{TMEDA}]\text{Cu}_2\text{Br}_4$, respectively, based on the Tauc's function, which are comparable to that of the most reported low-dimensional copper halides (Fig. S2–S4[†]). Under 254 nm UV light irradiation, all three halides exhibit bright blue light emission, and the photophysical properties of the three halides were subsequently studied at room temperature. As shown in Fig. 2a–c, the strongest photoluminescence excitation (PLE) peaks of the three halides is located at 286 nm, 295 nm and 301 nm for $[(\text{Me})_4\text{-Pipz}]\text{Cu}_2\text{Br}_4$, $[\text{BuDA}]\text{Cu}_2\text{Br}_4$ and $[\text{TMEDA}]\text{Cu}_2\text{Br}_4$, respectively. At the strongest excitation wavelength, the three halides show broadband emissions centered at 445 nm, 457 nm and 474 nm with full-width at half-maximum (FWHM) of 54 nm, 73 nm and 80 nm and Stokes shifts of 159 nm, 162 nm and 173 nm, respectively. The calculated CIE chromaticity coordinates were (0.15, 0.11), (0.15, 0.16) and (0.15, 0.23) for $[(\text{Me})_4\text{-Pipz}]\text{Cu}_2\text{Br}_4$, $[\text{BuDA}]\text{Cu}_2\text{Br}_4$ and $[\text{TMEDA}]\text{Cu}_2\text{Br}_4$, respectively, according to the PL emission spectra, which is located in the blue light region (Fig. 2d–f). The excitation wavelength-dependent PL spectra and emission wavelength-dependent PLE spectra were recorded to investigate the emission nature. As shown in Fig. S5–S7,[†] the three halides feature identical PL spectra under varied excitation wavelength and the PLE spectra also remain unchanged, indicating that the blue light emissions stem from the recombination of the same excited states, which were further confirmed by only one emitting center in the 3D consecutive PLE/PL maps (Fig. S8[†]).

Additionally, the finely ground microscale powders of the three halides also have sufficient emission intensity compared with the single crystals, ruling out the possibility of surface defect-induced emission (Fig. S9–S11[†]). The PL decay curves of the three halides were fitted by the biexponential function, which give an average PL lifetime of 7.1 μs , 12.2 μs and 15.6 μs for $[(\text{Me})_4\text{-Pipz}]\text{Cu}_2\text{Br}_4$, $[\text{BuDA}]\text{Cu}_2\text{Br}_4$ and $[\text{TMEDA}]\text{Cu}_2\text{Br}_4$, respectively, demonstrating the phosphorescence characteristics, resembling many reported low-dimensional Cu(I) halides (Fig. 2g–i).^{25–27} The photoluminescence quantum yield (PLQY) of the three halides were measured using the PL measurement system with the integrating sphere, which was calculate to be 37.8%, 13.6% and 10.3% for $[(\text{Me})_4\text{-Pipz}]\text{Cu}_2\text{Br}_4$, $[\text{BuDA}]\text{Cu}_2\text{Br}_4$ and $[\text{TMEDA}]\text{Cu}_2\text{Br}_4$, respectively (Fig. S12–S14[†]). These values are lower than those of some previously reported blue-emissive low-dimensional Cu(I)-based halides, such as $(\text{TPA})\text{CuBr}_2$,²⁸ $(\text{C}_8\text{H}_{20}\text{N})_2\text{Cu}_2\text{Br}_4$,²⁰ and $(\text{TEA})_2\text{Cu}_2\text{Br}_4$,²⁹ but higher than those of the 3D bulk materials $\text{Cs}_2\text{AgInCl}_6$,³⁰ $[(\text{Me})_2\text{-DABCO}]\text{Cu}_6\text{I}_8$ ³¹ and $[(\text{NH}_4)_2]\text{CuPbBr}_5$.³² Considering the large Stokes shift, wide FWHM and microsecond scale lifetime, these broadband blue light emissions can be ascribed to the radiative recombination of STEs resulting from the strong electro-phonon coupling, which is similar to those of various reported low-dimensional hybrid metal halides.^{33,34}

The temperature-dependent PL spectra of $[(\text{Me})_4\text{-Pipz}]\text{Cu}_2\text{Br}_4$ were recorded from 80 K to 300 K to further investigate

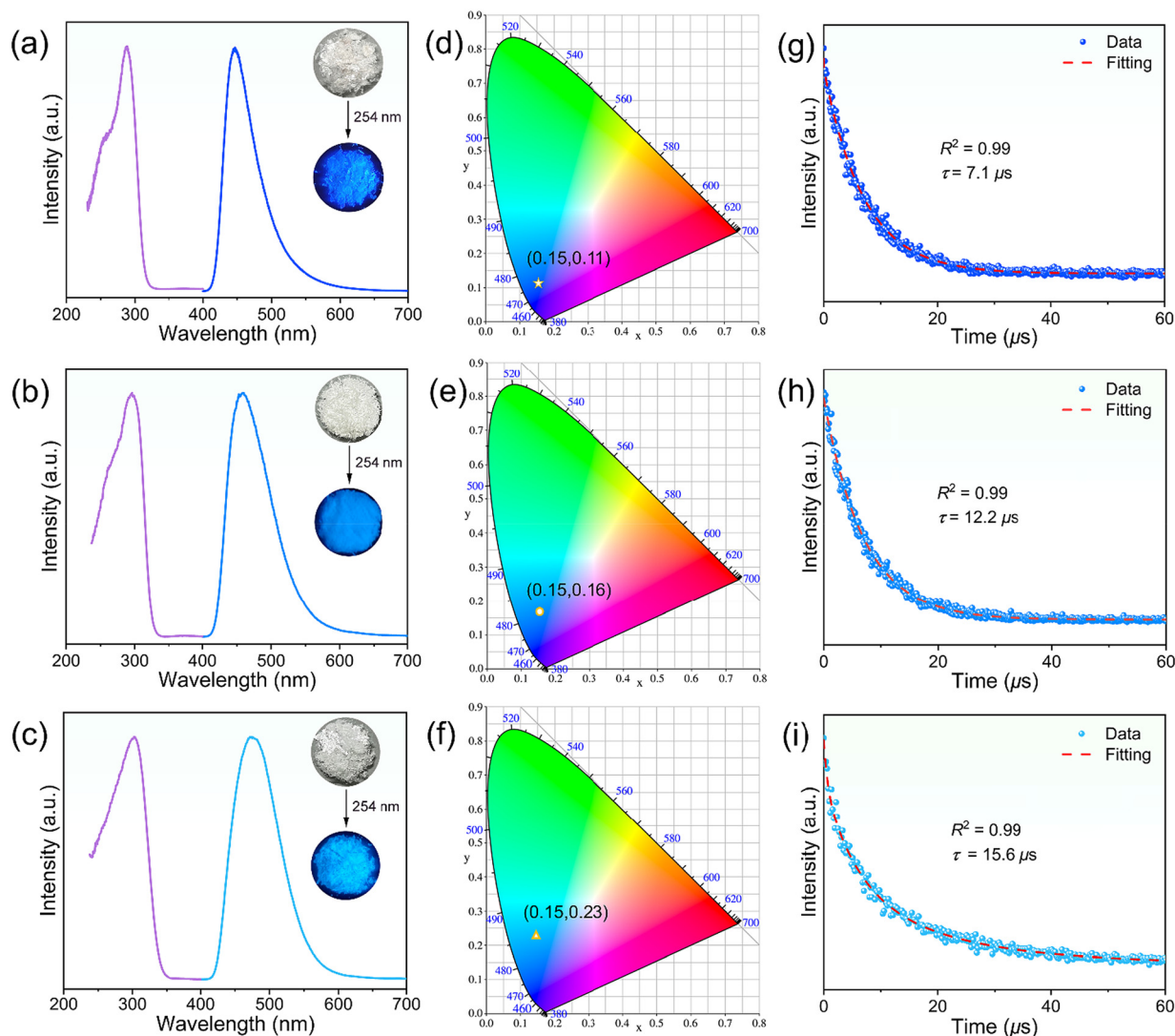


Fig. 2 The PL characterization of $[(\text{Me})_4\text{-Pipz}]\text{Cu}_2\text{Br}_4$ (up), $[\text{BuDA}]\text{Cu}_2\text{Br}_4$ (middle) and $[\text{TMEDA}]\text{Cu}_2\text{Br}_4$ (down): (a–c) PL excitation and emission spectra (inset: photographs of the crystals under sunlight and 254 nm UV light); (d–f) CIE coordinates; (g–i) PL decay curves at room temperature.

the mechanism of broadband blue light emission considering the highest PLQY. As shown in Fig. 3a and b, neither peak splitting nor the visible wavelength shift of the PL spectra was observed, indicating the single emission mechanism, which is consistent with the result from the wavelength-dependent PL and PLE measurement. In addition, the PL intensity increases monotonically along with decreasing temperature, which results from the weakened thermal vibration-induced non-radiative recombination. The thermal activation energy (E_a) can be calculated according to the Arrhenius formula to evaluate the excitation recombination degree as follows.

$$I_T = \frac{I_0}{1 + A \exp\left(-\frac{E_a}{k_B T}\right)}$$

where I_T and I_0 are the integrated PL intensities at T K and 0 K, respectively, E_a is the exciton binding energy, and k_B is the

Boltzmann constant. The E_a was calculated to be 126.9 meV, which is larger than the thermal decomposition energy of the free excitons (26 meV) at room temperature, indicating the formation of stable STEs (Fig. 3c). Additionally, the soft lattice in the crystals are more favourable for self-trapping exciton emission due to the strong coupling between the excitons and lattice vibration, which can be evaluated by Huang–Rhys factor (S) as follows.

$$\text{FWHM} = 2.36\sqrt{S}\hbar\omega_{\text{photon}} \sqrt{\coth\frac{\hbar\omega_{\text{photon}}}{2k_B T}}$$

where T is the temperature, S is the Huang–Rhys electron–phonon factor and $\hbar\omega_{\text{photon}}$ represents the phonon frequency. The S value was calculated to be 5.9, outperforming those of 3D perovskites (Fig. 3d). Generally speaking, the strong electron–phonon coupling can be verified when $S > 5$.^{35–37} Herein, 5.9 indicates that electron–phonon coupling exists in $[(\text{Me})_4\text{-Pipz}]\text{Cu}_2\text{Br}_4$.

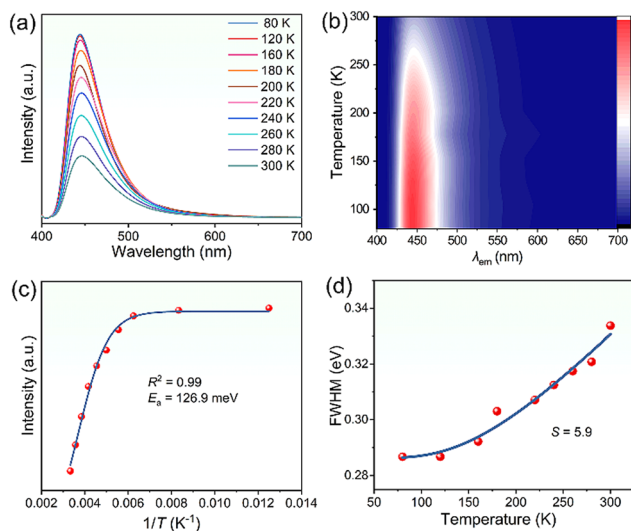


Fig. 3 (a) Temperature-dependent PL emission spectra. (b) Color mapping of temperature-dependent PL emission spectra. (c) Integrated PL intensity as a function of reciprocal temperature; (d) Fitted plot of PL FWHM versus the temperature of $[(\text{Me})_4\text{-Pipz}]\text{Cu}_2\text{Br}_4$.

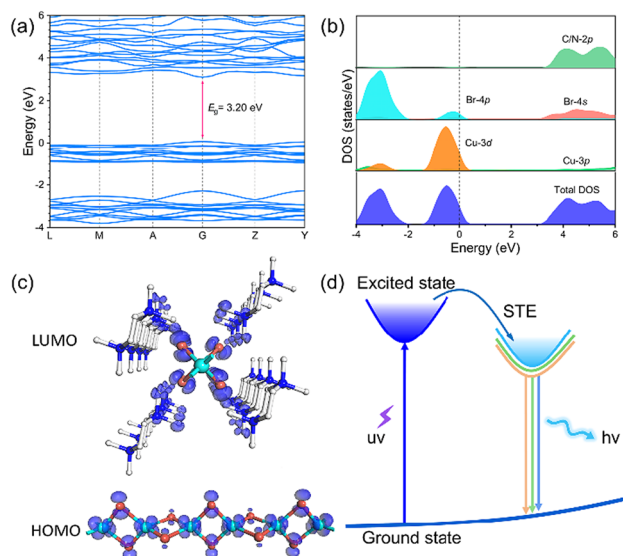


Fig. 4 (a) Calculated band structure and (b) DOS; (c) Charge density of HOMO and LUMO; (d) Configuration diagram of the emission process of $[(\text{Me})_4\text{-Pipz}]\text{Cu}_2\text{Br}_4$.

Cu_2Br_4 , which provides suitable conditions for luminescence derived from STEs or excited-state structural reorganization. Moreover, the phonon frequency $\hbar\omega_{\text{photon}}$ of 33.4 meV was obtained by fitting the Huang–Rhys factor, which is in good agreement with the Raman mode at 269.4 cm^{-1} (Fig. S15†).

The band structure and density of states (DOS) based on DFT were calculated to in-depth understand the electronic property of $[(\text{Me})_4\text{-Pipz}]\text{Cu}_2\text{Br}_4$. As shown in Fig. 4a, the band structure shows a direct band gap of 3.2 eV. This value is slightly lower than the result of 4.0 eV obtained from the experiment due to the underestimated bandgap for the semiconductor in the DFT study.^{38–40} In addition, the relatively flat valence band maximum (VBM) and conduction band minimum (CBM) indicate the weak electronic interactions between the adjacent cuprous bromide chains, further verifying the intensive quantum confinement effect and highly localized electrons in $[(\text{Me})_4\text{-Pipz}]\text{Cu}_2\text{Br}_4$. The total and partial density of states (DOS) are shown in Fig. 4b, the VBM is mainly contributed by the Cu 3d and Br 4p states, whereas the CBM is mainly composed of the Br 4s orbital. The negligible contribution of organic cations to both the CBM and VBM verifies the highly localized excitons on the cuprous bromide chains, which further confirm that the emission should come from the STEs on the $[\text{Cu}_2\text{Br}_4]^{2-}$ chains. Further, the charge density in the highest occupied molecular orbital (HOMO) and lowest unoccupied molecular orbital (LUMO) is overwhelmingly located on the $[\text{Cu}_2\text{Br}_4]^{2-}$ chains, validating the highly localized excitons (Fig. 4c). Based on the above experimental and theoretical investigations, we ascribe the broadband blue light emission to the STEs, which is similar to that of many reported 1D hybrid halides. The schematic diagram of the proposed photophysics process is depicted in Fig. 4d.^{41–43} Upon UV light excitation, the electrons at the ground states are

excited promptly to the excited states and then interact with phonon vibration to form self-trapped excitons due to the strong structural deformation at the excited state of the soft 1D crystal lattice. Subsequently, the excited electrons undergo intersystem crossing (ISC) from the singlet state to the triplet state as triplet STEs. Finally, the recombination from the STEs to the ground states gives rise to broadband light emission with a large Stokes shift.

Despite recent advances in the synthesis and application of optoelectronic devices, the inherent instability of metal halides on exposure to heat and moisture still restricts their practical applications, which must be overcome fundamentally. The encapsulating strategy has been developed to achieve the high stability of OIMHs, but it still suffers from the complicated synthetic process. Hence, designing and synthesizing metal halides with intrinsic stability at the molecular level is of great significance for their practical applications.^{44,45} A series of contrast experiments show that these 1D halides feature high thermal and chemical stabilities. As shown in Fig. S16,† the TGA curves indicate that the three halides can be stable up to about at least 250 °C with high thermal decomposition temperature. In addition, these halides exhibit high chemical stabilities in various organic solvents. As shown in Fig. S17–S19,† the PXRD patterns and PL emission spectra after soaking in various organic solvents remained unchanged compared to that of the as-synthesized sample, indicating the high tolerance for these polar organic solvents. After exposure to humid air for one month, the PXRD pattern remained consistent with that of the as-synthesized sample and the PL emission intensity only reduced by 9.4%, demonstrating high stability in the atmospheric environment (Fig. S9†).

More interestingly, $[(\text{Me})_4\text{-Pipz}]\text{Cu}_2\text{Br}_4$ exhibits extraordinary anti-water stability besides the chemical and thermal

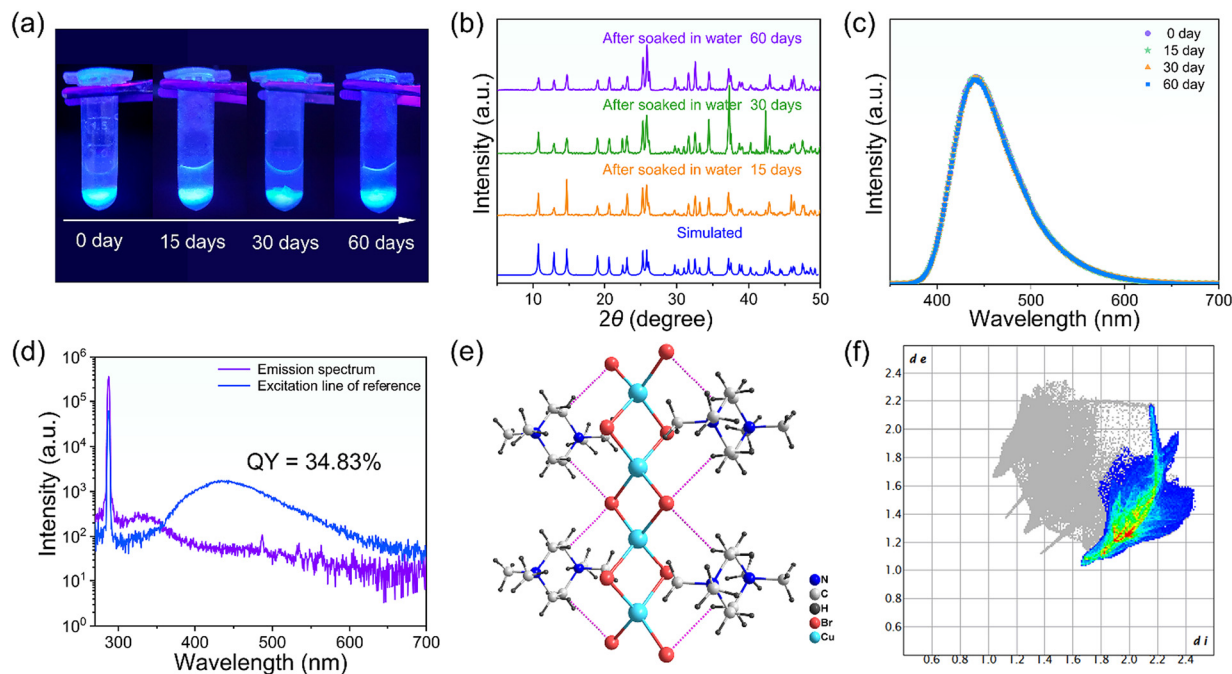


Fig. 5 Anti-water stability of $[(\text{Me})_4\text{-Pipz}]\text{Cu}_2\text{Br}_4$. (a) Optical images of the crystals in deionized water under a 254 nm UV lamp; (b) PXRD patterns and (c) PL spectra after soaking in water at different periods; (d) PLQY after soaking in water for two months. (e) Hydrogen bonding interactions between the 1D $[\text{Cu}_2\text{Br}_4]^{2-}$ chain and $[(\text{Me})_4\text{-Pipz}]^{2+}$ cation; (f) 2D fingerprint plot analysis of weak hydrogen bonds in the crystal structure.

stabilities. As shown in Fig. 5a, $[(\text{Me})_4\text{-Pipz}]\text{Cu}_2\text{Br}_4$ can still maintain the original shape and bright blue light emission even after continuous immersion in water for over two months. To further verify the structural stability, the PXRD pattern of the sample after soaking in water for two months was recorded. As shown in Fig. 5b, the PXRD pattern after soaking in water is in accordance with that of the initial sample, indicating no structural degradation and ultra-high stability in water. Fig. 5c shows the PL spectra before and after immersing the sample in water for different times, which exhibits the same spectral profile. We performed inductively-coupled plasma mass spectrometry (ICP-MS) for the residual solution after removing the sample, and the result indicates that negligible Cu^+ dissolves in water with a low mass concentration of 21 ppm, showing almost no Cu^+ leaching in the experimental process. Besides, the PL intensity reduces only 4.5% after two months compared to that of the pristine sample. Meanwhile, the PLQY of 34.8% is still close to that of the as-synthesized sample, further demonstrating the high anti-water stability (Fig. 5d). The anti-water stability of these 1D halides are comparable with those of previously reported Zn^{2+} , Cu^+ and Sn^{3+} -based halides, such as $(\text{C}_4\text{H}_9)_4\text{NCuCl}_2$,⁴⁶ $(\text{C}_{20}\text{H}_{20}\text{OP})\text{CuCl}_2$,²³ $(1,3\text{-dppH}_2)_2\text{Cu}_4\text{I}_8\cdot\text{H}_2\text{O}$ ⁴⁷ and $(\text{TBP})_2\text{SnCl}_6$,⁴⁸ further confirming the potential applications under extreme conditions. To deeply understand the nature of the ultra-high anti-water stability of $[(\text{Me})_4\text{-Pipz}]\text{Cu}_2\text{Br}_4$, Hirshfeld surface calculation was performed to analyze the intermolecular force between the $[\text{CuBr}_4]^{2-}$ and $[(\text{Me})_4\text{-Pipz}]^{2+}$ components using the CrystalExplorer software. As shown in Fig. 5e and f, abundant

hydrogen bonds of $\text{C-H}\cdots\text{Br}$ between $[\text{CuBr}_4]^{2-}$ and $[(\text{Me})_4\text{-Pipz}]^{2+}$ were found with the proportion of 67.6% in all the weak intermolecular force of $[(\text{Me})_4\text{-Pipz}]\text{Cu}_2\text{Br}_4$, strengthening the interactions between the $[\text{CuBr}_4]^{2-}$ anions and $[(\text{Me})_4\text{-Pipz}]^{2+}$ cations, which is favourable for the high structural stability. In the crystal structure, the closely arranged $[(\text{Me})_4\text{-Pipz}]^{2+}$ cations form a dense “shell” to tightly wrap the inorganic skeleton. Thus, the large amount of hydrogen bonds and separating effect from the organic component can protect the inorganic skeleton, further enhancing the anti-water stability as well as the thermal and chemical stabilities.^{49,50}

3. Conclusions

In conclusion, we reported a series of isostructural 1D hybrid cuprous bromides based on the same $[\text{Cu}_2\text{Br}_4]^{2-}$ chain from the edge-shared $[\text{CuBr}_4]$ tetrahedron. These copper(i) halides emit bright blue light with the highest PLQY of 37.8% from the intrinsic STEs. In addition, the halide shows ultra-high anti-water stability without structure degradation and PL quenching in water for at least two months, which is attributed to the protection of organic cations. Hirshfeld surface analysis shows that the large amount of hydrogen bonds does not only enhance the interactions between the organic cations and inorganic skeleton but also protects the inorganic skeleton in water and other extreme conditions. This work may extend the applications of low-dimensional organic-inorganic hybrid halides in extreme environments such as underwater lighting.

4. Experimental

Materials

All chemicals used in the reactions were commercially available and used directly without further purification. CuBr (99%, Aladdin), hydrobromic acid (40%, Aladdin), methanol (98%, Aladdin), ethanol (98%, Aladdin), aqueous hypophosphoric acid solution (50%, Aladdin) and aqueous HCl solution (37%, Aladdin).

Synthesis of [(Me)₄Pipz]Cu₂Br₄

CuBr (1 mmol, 0.143 g) and piperazine (1 mmol, 0.086 g) were dissolved in methanol (4 mL), DMF (1 mL), hydrobromic acid (1 mL) and hypophosphoric acid (0.5 mL). The mixture was sealed in a 25 mL Teflon-lined stainless-steel reactor and heated at 140 °C for 5 days. After cooling to room temperature, colourless plate crystal of [(Me)₄Pipz]Cu₂Br₄ (yield based on CuBr, 58%) was obtained. Elemental analysis (%): calcd: C 16.26, N 4.74, H 3.41; found: C 16.14, N 4.76, H 3.48.

Synthesis of [BuDA]Cu₂Br₄

CuBr (1 mmol, 0.143 g) and BuDA (1 mmol, 0.088 g) were dissolved in ethanol (4 mL), hydrobromic acid (1 mL) and hypophosphoric acid (0.5 mL). The mixture was sealed in a 20 mL glass bottle and heated at 80 °C for 5 days. After cooling to room temperature, colourless block crystals of [BuDA]Cu₂Br₄ (yield based on CuBr, 58%) were obtained. Elemental analysis (%): calcd: C 8.94, N 5.22, H 2.63; found: C 8.83, N 5.31, H 2.78.

Synthesis of [TMEDA]Cu₂Br₄

The synthesis process of [TMEDA]Cu₂Br₄ is similar to that of [BuDA]Cu₂Br₄ except that 1 mmol BuDA was replaced by 1 mmol TMEDA (yield based on CuBr, 80%). Elemental analysis (%): calcd: C 12.76, N 4.96, H 3.21; found: C 12.71, N 4.98, H 3.29.

Characterization

The single crystal data were collected on a Bruker X-ray diffractometer (SMART II, Mo-K α , λ = 0.71073 Å) at 298 K. The structure was solved by direct methods and refined on F^2 by full-matrix least-squares method using the SHELXL-2018 program. Basic information pertaining to crystal parameters and structure refinement is summarized in Table S1.†

Powder X-ray diffraction (PXRD) data were obtained using a Bruker D8 ADVANCE powder X-ray diffractometer (Cu K α , λ = 1.5418 Å) in the 2θ range of 5–50°. UV-vis absorption was measured directly on ground single crystals with BaSO₄ as the substrate in the wavelength range of 200–1000 nm on a PE Lambda 900 UV-vis spectrophotometer. Thermogravimetric analysis (TGA) was done on a Mettler TGA/SDTA 851 thermal analyzer under a N₂ atmosphere with a heating rate of 10 °C min⁻¹ from 25 °C to 800 °C.

Characterization of the photoluminescence property

The PL excitation and emission spectra were recorded on an Edinburgh FLS980 fluorescence spectrometer.

The PLQY was determined on an FLS980 fluorescence spectrometer with an integrating sphere in the solid state, utilizing a 450 W xenon lamp with an excitation power of 600 μ W cm⁻² as the light source.

Calculation of PLQY. $\eta_{\text{QE}} = I_{\text{S}}/(E_{\text{R}} - E_{\text{S}})$ was employed to calculate the value of PLQY, where I_{S} is the sample's luminescence emission spectrum, E_{S} is the wavelength of the integrating sphere's excitation light spectrum (without the sample), and E_{R} is the sample's excitation spectrum.

Theoretical calculation

Theoretical calculations were performed using the CASTEP program based on the density functional theory (DFT), and the single crystal data was directly used as the structural model. The normal conservation pseudopotentials were utilized to describe the interaction between the core and outer electrons. As a result, the employed valence electrons were C 2s²2p², N 2s²2p³, H 1s¹, Cu 3d¹⁰4s¹ and Br 4s²4p⁵. Other calculation parameters and convergence criteria used the default settings of the CASTEP code.

Data availability

Crystallographic data for [(Me)₄Pipz]Cu₂Br₄, [BuDA]Cu₂Br₄ and [TMEDA]Cu₂Br₄ have been deposited at the Cambridge Crystallographic Data Centre with deposition numbers CCDC: 2367415, 2367417 and 2367419,† respectively. Additional characterizations of three compounds, including UV-vis absorption spectra, PLQY, TGA, PL spectroscopy data, and solvent stability characterization are provided in the ESI.†

Conflicts of interest

The authors declare no conflict of interest.

Acknowledgements

We express thanks for financial support from the National Nature Science Foundation of China (22171105), Shandong Provincial Natural Science Foundation (ZR2022YQ14 and ZR2021MB001) and Special Foundation of Taishan Scholar Project.

References

- 1 D. Chen, J. Li, X. Chen, J. Chen and J. Zhong, *ACS Appl. Mater. Interfaces*, 2019, **11**, 10059–10067.
- 2 A. Pan, M. Jurow, Y. Zhao, F. Qiu, Y. Liu, J. Yang, J. J. Urban, L. He and Y. Liu, *Nanoscale*, 2017, **9**, 17688–17693.
- 3 Y.-Y. Guo and P. Lightfoot, *Dalton Trans.*, 2020, **49**, 12767–12775.
- 4 S. Seth, T. Ahmed, A. De and A. Samanta, *ACS Energy Lett.*, 2019, **4**, 1610–1618.

- 5 X. Meng, S. Ji, Q. Wang, X. Wang, T. Bai, R. Zhang, B. Yang, Y. Li, Z. Shao, J. Jiang, K.-L. Han and F. Liu, *Adv. Sci.*, 2022, **9**, 2203596.
- 6 N. Lin, R.-C. Wang, S.-Y. Zhang, Z.-H. Lin, X.-Y. Chen, Z.-N. Li, X.-W. Lei, Y.-Y. Wang and C.-Y. Yue, *Laser Photonics Rev.*, 2023, **17**, 2300427.
- 7 T. Huang, Q. Wei, T. Li, Q. Niu, W. Li, G. Huang and B. Zou, *Adv. Opt. Mater.*, 2024, **12**, 2302384.
- 8 Z. Wang, X. Chen, Y. Song, Z. Du, Y. Zhou, M. Li, W. Huang, Q. Xu, Y. Li, S. Zhao and J. Luo, *Angew. Chem., Int. Ed.*, 2023, **62**, e202311086.
- 9 N. Sun, J. Lin, S. He, J. Cao, Z. Guo, J. Zhao, Q. Liu and W. Yuan, *Inorg. Chem.*, 2023, **62**, 3018–3025.
- 10 X.-W. Kong, L.-X. Wu, X. Yang, D.-Y. Wang, S.-X. Wang, S.-Y. Li, C.-Y. Yue, F. Yu and X.-W. Lei, *Adv. Opt. Mater.*, 2024, **12**, 2302710.
- 11 H.-J. Yang, W. Xiang, X. Zhang, J.-Y. Wang, L.-J. Xu and Z.-N. Chen, *J. Mater. Chem. C*, 2024, **12**, 438–442.
- 12 Z. Hua, A. Ben-Akacha, Q. He, T. Liu, G. Boyce, M. van Deventer, X. Lin, H. Gao, B. Ma and P. Xiong, *ACS Energy Lett.*, 2022, **7**, 3753–3760.
- 13 C. Sun, J.-P. Zang, Y.-Q. Liu, Q.-Q. Zhong, X.-X. Xing, J.-P. Li, C.-Y. Yue and X.-W. Lei, *CCS Chem.*, 2022, **4**, 3106–3121.
- 14 W. Wang, C.-D. Liu, X.-B. Han, C.-Q. Jing, C.-Y. Chai, C.-C. Fan, M.-L. Jin, J.-M. Zhang and W. Zhang, *ACS Mater. Lett.*, 2024, **6**, 203–211.
- 15 W. Huang, X. Wu, B. Ahmed, Y. Li, Y. Zhou, H. Wang, Y. Song, X. Kuang, J. Luo and S. Zhao, *Inorg. Chem. Front.*, 2023, **10**, 2039–2044.
- 16 J.-H. Wei, W.-T. Ou, J.-B. Luo and D.-B. Kuang, *Angew. Chem., Int. Ed.*, 2022, **61**, e202207985.
- 17 S. Fang, A. Du, B. Zhou, Z. Liu, J. Nie, Y. Wang, H. Zhong, H. Hu, H. Li and Y. Shi, *Adv. Opt. Mater.*, 2023, **11**, 2202952.
- 18 H. Peng, X. Wang, Y. Tian, B. Zou, F. Yang, T. Huang, C. Peng, S. Yao, Z. Yu, Q. Yao, G. Rao and J. Wang, *ACS Appl. Mater. Interfaces*, 2021, **13**, 13443–13451.
- 19 T.-L. Yu, Y.-M. Guo, G.-X. Wu, X.-F. Yang, M. Xue, Y.-L. Fu and M.-S. Wang, *Coord. Chem. Rev.*, 2019, **397**, 91–111.
- 20 B. Su, J. Jin, K. Han and Z. Xia, *Adv. Funct. Mater.*, 2023, **33**, 2210735.
- 21 L. Lian, X. Wang, P. Zhang, J. Zhu, X. Zhang, J. Gao, S. Wang, G. Liang, D. Zhang, L. Gao, H. Song, R. Chen, X. Lan, W. Liang, G. Niu, J. Tang and J. Zhang, *J. Phys. Chem. Lett.*, 2021, **12**, 6919–6926.
- 22 F. Liu, P. Hao, T. Yu, Q. Guan and Y. Fu, *J. Mol. Struct.*, 2016, **1119**, 431–436.
- 23 D. Huang, C. Cao, H. Cheng, D. Wang, W. Yang and R. Xie, *Mater. Today Chem.*, 2024, **37**, 102010.
- 24 R.-Y. Wang, X. Zhang, Q.-S. Huo, J.-H. Yu and J.-Q. Xu, *RSC Adv.*, 2017, **7**, 19073–19080.
- 25 S. Zhao, J. Zhao, S. M. H. Qaid, D. Liang, K. An, W. Cai, Q. Qian and Z. Zang, *Appl. Phys. Rev.*, 2024, **11**, 011408.
- 26 Z. Song, Z. Jia, X. Guo, B. Yu, G. Liu, L. Meng, Y. Liu, Q. Lin and Y. Dang, *Adv. Opt. Mater.*, 2023, **11**, 2203014.
- 27 Y. Li, Z. Zhou, F. K. Sheong, Z. Xing, K. S. Wong, H. H. Y. Sung, I. D. Williams and J. E. Halpert, *Chem. Mater.*, 2023, **35**, 1318–1324.
- 28 Y. Tian, H. Peng, Q. Wei, Y. Chen, J. Xia, W. Lin, C. Peng, X. He and B. Zou, *Chem. Eng. J.*, 2023, **458**, 141436.
- 29 X. Liu, F. Yuan, C. Zhu, J. Li, X. Lv, G. Xing, Q. Wei, G. Wang, J. Dai, H. Dong, J. Xu, B. Jiao and Z. Wu, *Nano Energy*, 2022, **91**, 106664.
- 30 W. Ma, H. Wu, X. Liu, R. Miao, T. Liang and J. Fan, *Adv. Opt. Mater.*, 2022, **10**, 2200837.
- 31 H.-M. Pan, K. Xu, F.-L. Meng, H. Ge, X. Yin, X.-M. Wu, X.-W. Lei, Z.-H. Jing and C.-Y. Yue, *Inorg. Chem.*, 2021, **60**, 16906–16910.
- 32 C. Sun, Y.-H. Guo, S.-S. Han, J.-Z. Li, K. Jiang, L.-F. Dong, Q.-L. Liu, C.-Y. Yue and X.-W. Lei, *Angew. Chem., Int. Ed.*, 2020, **59**, 16465–16469.
- 33 Q. Hu, J. Liu, H. Yu, H. Xu, J. Yu and W. Wu, *Chem. Commun.*, 2023, **59**, 3763–3766.
- 34 T. Xu, Y. Li, M. Nikl, R. Kucerkova, Z. Zhou, J. Chen, Y.-Y. Sun, G. Niu, J. Tang, Q. Wang, G. Ren and Y. Wu, *ACS Appl. Mater. Interfaces*, 2022, **14**, 14157–14164.
- 35 J.-F. Liao, Z. Zhang, L. Zhou, Z. Tang and G. Xing, *Angew. Chem., Int. Ed.*, 2024, **63**, e202404100.
- 36 Z. Ma, X. Ji, S. Lin, X. Chen, D. Wu, X. Li, Y. Zhang, C. Shan, Z. Shi and X. Fang, *Adv. Mater.*, 2023, **35**, 2300731.
- 37 Y. Hui, S. Chen, R. Lin, W. Zheng and F. Huang, *Mater. Chem. Front.*, 2021, **5**, 7088–7107.
- 38 J. P. Perdew and M. Levy, *Phys. Rev. Lett.*, 1983, **51**, 1884–1887.
- 39 L.-K. Wu, R.-F. Li, W.-Y. Wen, Q.-H. Zou, H.-Y. Ye and J.-R. Li, *Inorg. Chem. Front.*, 2023, **10**, 3297–3306.
- 40 S. A. Novikov, A. D. Valueva and V. V. Klepov, *Dalton Trans.*, 2024, **53**, 12442–12449.
- 41 G. Wu, C. Zhou, W. Ming, D. Han, S. Chen, D. Yang, T. Besara, J. Neu, T. Siegrist, M.-H. Du, B. Ma and A. Dong, *ACS Energy Lett.*, 2018, **3**, 1443–1449.
- 42 B. Yang, L. Yin, G. Niu, J.-H. Yuan, K.-H. Xue, Z. Tan, X.-S. Miao, M. Niu, X. Du, H. Song, E. Lifshitz and J. Tang, *Adv. Mater.*, 2019, **31**, 1904711.
- 43 Z. Qi, Y. Chen, H. Gao, F.-Q. Zhang, S.-L. Li and X.-M. Zhang, *Sci. China: Chem.*, 2021, **64**, 2111–2117.
- 44 S. Zhou, Y. Chen, K. Li, X. Liu, T. Zhang, W. Shen, M. Li, L. Zhou and R. He, *Chem. Sci.*, 2023, **14**, 5415–5424.
- 45 J.-H. Wei, Y.-W. Yu, J.-B. Luo, Z.-Z. Zhang and D.-B. Kuang, *Adv. Opt. Mater.*, 2022, **10**, 2200724.
- 46 H. Peng, X. Wang, Y. Tian, T. Dong, Y. Xiao, T. Huang, Y. Guo, J. Wang and B. Zou, *J. Phys. Chem. Lett.*, 2021, **12**, 6639–6647.
- 47 B. Su, J. Jin, Y. Peng, M. S. Molokeev, X. Yang and Z. Xia, *Adv. Opt. Mater.*, 2022, **10**, 2102619.
- 48 B. Ke, H. Peng, Q. Wei, C. Yang, X. Li, W. Huang, Z. Du, J. Zhao and B. Zou, *Adv. Opt. Mater.*, 2024, **12**, 2301665.
- 49 Y.-H. Liu, X. Yan, L. Xiao, W. Jiang, Q. Liu, T.-C. Liu, T.-Y. Yan, C.-Y. Yue and X.-W. Lei, *Adv. Opt. Mater.*, 2023, **11**, 2301010.
- 50 Q. Ba, A. Jana, L. Wang and K. S. Kim, *Adv. Funct. Mater.*, 2019, **29**, 1904768.